RSC Advances

ROYAL SOCIETY OF CHEMISTRY

www.rsc.org/advances

Novel synthesis of $Mn_3(PO_4)_2 \cdot 3H_2O$ nanoplate as a precursor to fabricate high performance $LiMnPO_4$/C composite for lithium-ion batteries

Kaipeng Wu, Guorong Hu*, Zhongdong Peng, Zhijian Zhang, Yanbing Cao, Ke Du

School of Metallurgy and Environment, Central South University,

Changsha 410083, China

*Corresponding author, E-mail: hgrhsj@263.net, Tel: +86 15084864373.

Abstract

$Mn_3(PO_4)_2 \cdot 3H_2O$ precursor was synthesized by a novel precipitation process using ethanol as initiator, and was lithiated to $LiMnPO_4$/C composite via a combination of wet ball-milling and heat treatment. The as-synthesized precursor was in plate-shape with nanosize thickness. After heat treatment of the ball-milled mixture of $Mn_3(PO_4)_2 \cdot 3H_2O$, $NH_4H_2PO_4$, Li_2CO_3 and glucose, the well crystallized and highly pure $LiMnPO_4$ with the particle size of about 100 nm and the carbon coating layer of 2 nm was obtained. The $LiMnPO_4$/C composite fabricated at 650℃ delivers discharge capacities of 141.7 mAh g^{-1} at 0.05 C, 119.9 mAh g^{-1} at 1 C and 88.7 mAh g^{-1} at 5 C. Meanwhile, it can retain 95.2% of the initial capacity after 100 cycles at 0.5C, revealing a quite good cycling stability. The method described in this work can be helpful in the development of $LiMnPO_4$/C cathode materials for advanced Lithium-ion batteries.

Key Words: Precipitation method; Manganese (II) phosphate trihydrate nanoplates; Lithium manganese phosphate; Cathode materials; Lithium-ion battery.

1. Introduction

Currently, the olivine structured lithium transition metal phosphate $LiMPO_4$ (M = Fe, Mn) are receiving much attention for lithium ion batteries cathode due to their low cost, environmental friendliness, as well as electrochemical and thermal stability [1-3]. In fact, $LiFePO_4$ has been widely studied and commercially applied in large-scale transportation and energy storage. However, $LiFePO_4$ is known to have low energy density (586 Wh kg^{-1}) due to its low voltage plateau (3.4 V vs. Li/Li^+), which prevents it from wider acceptance for vehicle application [4-6]. In consideration of the higher energy density, a number of studies on $LiMnPO_4$ have been reported due to its higher intercalation potential at 4.1 V versus Li/Li^+, which makes the theoretical energy density is about 1.2 times larger than that of $LiFePO_4$, and is compatible with most of the current organic electrolyte systems presently used in lithium-ion batteries [7-9].

However, $LiMnPO_4$ has low Li-ions diffusion kinetics in the crystals, which leads to poor electrochemical activities [10,11]. So far, considerable efforts have been made to overcome this problem, such as doping metal ions, reducing the particle size and coating conductive carbon layer [12-14]. Furthermore, various synthetic methods have been developed to prepare carbon-coated $LiMnPO_4$ such as sol-gel [15,16], hydrothermal [17,18], solvothermal [19-21] and precipitation method [22,23]. Of the reported methods, the Mn-P precursor-based precipitation method is a commercially viable one due to its simplicity as well as suitable for scale-up production [24,25]. Moreover, it is generally accepted that using Mn-P precursor to fabricate $LiMnPO_4$ is greatly helpful to the uniformity of $LiMnPO_4$ when a simple solid-state reaction

method is employed and the electrochemical performances of $LiMnPO_4$/C composite are closely associated with characteristics (such as morphology, particle size and distribution) of the precursors [26,27]. Liu [28] prepared flower-like $NH_4MnPO_4 \cdot H_2O$ as the precursor to synthesis $LiMnPO_4$ which preserved the morphology of the precursor. This material delivers poor discharge capacity of 85 mAh g^{-1} at 0.05 C. Zhu [29] synthesized $LiMnPO_4$/C nano-composite from manganese (II) phosphate trihydrate precipitated from a micro-channel reactor approach. The composite could deliver discharge capacities of 137, 106.8, 70 and 43.1 mAh g^{-1} at 0.05, 0.1, 0.5 and 1 C, respectively. Cao [30] used the 100~300 nm petal shaped $MnPO_4 \cdot H_2O$ precipitate as the precursor to prepare 20~50 nm $LiMnPO_4$/C nano-composites by mechanochemical activation assisted with a carbothermal reduction route. The carbon coated $LiMnPO_4$/C could display discharge specific capacities of 124 mAh g^{-1} at 0.05 C and 108 mAh g^{-1} at 1 C. In spite of these efforts, the traditional precipitation methods to prepare the Mn-P precursor were reported to be time consuming and demand strict reaction conditions (such as time, temperature, pH value and additives.). Moreover, toxic gases, such as NO_2 and NO, are released from the synthesis process [30]. Therefore, a facile and fast solution-based procedure is still highly desirable for preparation of Mn-P precursor to fabricate $LiMnPO_4$/C cathode materials.

Keeping this in mind, we present here a facile process for the synthesis of well-crystallized $Mn_3(PO_4)_2 \cdot 3H_2O$ by a novel precipitation process using ethanol as initiator. Compared with the traditional co-precipitation and homogeneous precipitation method, the way reported here is fundamentally different due to its

noninvolvement of any pH regulator and heating device which is suitable for scale-up production. Subsequently, the pre-synthesized $Mn_3(PO_4)_2 \cdot 3H_2O$ was used as a Mn-P precursor to fabricate $LiMnPO_4$/C cathode material by a combination of wet ball-milling and heat treatment. During the heat treatment process, the morphology of $Mn_3(PO_4)_2 \cdot 3H_2O$ precursor could be easily destroyed due to the instability of nanoplates under high temperature condition, and the particle size of $LiMnPO_4$/C could be controlled within 150 nm. Moreover, the sintering temperature of $LiMnPO_4$/C was optimized. The fabricated $LiMnPO_4$/C composite displays excellent rate performance and cycling stability.

2. Experimental

2.1. Sample preparation

The precursor was synthesized by a novel precipitation method using $MnSO_4 \cdot H_2O$ and $NH_4H_2PO_4$ as raw materials. In a typical synthetic procedure, $MnSO_4 \cdot H_2O$ (0.1 mol) and $NH_4H_2PO_4$ (0.1 mol) were dissolved in 100mL distilled water under stirring to give a homogeneous solution. Then, anhydrous ethanol (250 mL) was dropped quickly into the solution under vigorous stirring and stirred for 1h. Then, the pale-pink precipitation was collected by centrifugation, washed sequentially by distilled water and dried in an oven at 80℃ for 12 h. Subsequently, the obtained $Mn_3(PO_4)_2 \cdot 3H_2O$ precursor, $NH_4H_2PO_4$, Li_2CO_3 and glucose with the molar ratio of 1:1:1.5:0.58 were mixed in ethanol medium under ball milling for 4h. The mixture was dried overnight and then sintered at 550, 600, 650 and 700℃ for 6 h in an Ar atmosphere. Finally, $LiMnPO_4$/C composite was obtained. The carbon contents of

$LMnPO_4/C$ sintered at 550, 600, 650 and 700℃ are 6.74 wt%, 6.70 wt%, 6.68 wt% and 6.65 wt%, respectively.

2.2. Sample analysis

The crystalline structures of all samples were analyzed by the powder X-ray diffraction (XRD, D/max-r A type Cu Kα, 40 kV, 300 mA, 10-80°). The morphologies were observed using scanning electron microscope (SEM, JEOL, JSM-6360LV) and transmission electron microscope (TEM, JEOL, JEM-2010FEF). Raman spectra were collected on a Raman spectrometer (Renishaw inVia Ramdan microscope with 633 nm excitation laser). The TGA/DSC analysis was determined by a NETZSCH STA-449C (Germany) with a heating rate of 5℃ min^{-1} under argon atmosphere. The specific surface area was measured using the BET method. The content of carbon was determined by infrared C-S analysis equipment (HW 2000).

2.3. Electrochemical measurement

The electrochemical performance was evaluated using 2025 coin cells with metallic lithium as the counter electrode, Celgard 2400 as the separator and 1 M $LiPF_6$ dissolved in EC+DMC (1:1 in volume) as the electrolyte. The test electrodes were built by mixing the $LiMnPO_4/C$, black carbon, and PVDF binder in a weight ratio of 80:10:10. These were then pasted onto an Al foil current collector and dried at 120 ℃ for 6 h in a vacuum oven. Then, it was cut into rounded pieces with a diameter of 10 mm. The active material on each piece weighed about 1.8 mg. The test cells were assembled in an argon filled glove box. The cells were charged in a CC-CV mode (galvanostatically charged to 4.5 V at a rate of 0.05C (1C=170 mAh g^{-1}), then

potentiostatically charged at 4.5 V till current drops to 0.01C), and then discharged to 2.5 V at a specific rate using a battery test system (Land CT 2001A, Land Co. China). Cyclic voltammetry (CV) curves were recorded in the voltage region of 2.5-4.5 V with Model 2273A Electrochemical Instruments (PerkinElmer Co., USA) at various scanning rates.

3. Results and discussion

$Mn_3(PO_4)_2 \cdot 3H_2O$ precursor was innovatively synthesized via a facile precipitation process. Fig. 1a presents the XRD pattern of the precursor, where the as-synthesized precursor exhibited a prismatic crystal system belonging to a space group of P21/a. The relative intensities and positions of all the diffraction peaks of the precursor match well with standard $Mn_3(PO_4)_2 \cdot 3H_2O$ (JCPDS: 03-0426). The sharp characteristic peaks demonstrate that $Mn_3(PO_4)_2 \cdot 3H_2O$ possesses high crystallinity. In addition, the Mn/P mole ratio of $Mn_3(PO_4)_2 \cdot 3H_2O$ was determined by chemical titration to be 1.496, which is close to the stoichiometric ratio of the $Mn_3(PO_4)_2 \cdot 3H_2O$. Based on these results, it proved that $Mn_3(PO_4)_2 \cdot 3H_2O$ can be innovatively prepared by the proposed method. Meanwhile, during the preparation process, the reactions may occur as follows:

$$H_2PO_4^- \Leftrightarrow HPO_4^{2-} + H^+ \Leftrightarrow PO_4^{3-} + 2H^+ \quad (1)$$

$$3Mn^{2+} + 2PO_4^{3-} + 3H_2O \rightarrow Mn_3(PO_4)_2 \cdot 3H_2O\downarrow \quad (2)$$

According to the classical precipitation theory, the precipitation of nanoparticles proceeds in steps of generation of supersaturation, nucleation, and particle growth, followed by agglomeration in case of uncontrolled growth [31]. The main driving

force for precipitation is rapid and high supersaturation, which determines the final particle size of the precipitates. As for the preparation of nano-$Mn_3(PO_4)_2 \cdot 3H_2O$, after mixing the $MnSO_4 \cdot H_2O$ and $NH_4H_2PO_4$ in distilled water, a homogeneous aqueous solution was obtained. And the pH value of the solution was less than 4 due to the double-ionization of $H_2PO_4^-$ shown in equation (1). In these conditions, $Mn_3(PO_4)_2 \cdot 3H_2O$ could not precipitate from the solution [29]. After quick addition of anhydrous ethanol into the solution, the solubility of $Mn_3(PO_4)_2 \cdot 3H_2O$ in the mixed solvent (formed by water and ethanol in any ratio) decreased drastically due to the insoluble nature of the $Mn_3(PO_4)_2 \cdot 3H_2O$ in alcohol, which would generate the high supersaturation, leading to a much greater nucleation rate than growth as well as yielding the $Mn_3(PO_4)_2 \cdot 3H_2O$ precipitate with small particle size based on the reaction equation (2). Based on this, the rapid formation of the high supersaturation was induced by the addition of anhydrous ethanol. Thus, ethanol in this synthetic process was named an initiator. Nevertheless, the concrete mechanisms involved in this process remain to be investigated in further studies. Shown in Fig. 1b is the SEM image of prepared $Mn_3(PO_4)_2 \cdot 3H_2O$, the particles exhibit an irregular plate-shape with an average width and thickness of about 1um and 5 nm, respectively. No obvious agglomeration of $Mn_3(PO_4)_2 \cdot 3H_2O$ particles are observed, probably due to the specific morphology and the synthetic environment that offered by the water-ethanol medium.

Fig. 2a shows the TGA-DSC curves of the ball-milled mixture of $Mn_3(PO_4)_2 \cdot 3H_2O$, $NH_4H_2PO_4$, Li_2CO_3 and glucose. The TGA curve exhibits three

main stages of weight loss. In the first stage, a 3.5 wt% mass loss is found when heated from ambient temperature to 170℃, which is mainly ascribed to the elimination of physical water in mixture. Further mass loss of 17.4 wt% is observed between 170 and 310℃ with an exothermic peak detected at 190℃ in the DSC curve, which can be attributed to the removal of crystallized water from $Mn_3(PO_4)_2 \cdot 3H_2O$, the thermal decomposition of the glucose and the liberation of H_2O, CO_2 and NH_3 from the reaction of $NH_4H_2PO_4$ and Li_2CO_3 to form Li_3PO_4. A continuous weight loss (3 wt%), appeared from 310 to 600℃, is related to the continuous thermal decomposition of glucose. Moreover, a small exothermic peak is observed near 450℃ in the DSC curve, which can be ascribed to the formation of the crystalline phase of $LiMnPO_4$. There is almost no weight loss after 600℃, which indicated the crystallization process of $LiMnPO_4$ is completed. Based on these results, we choose 550, 600, 650 and 700℃ as sintering temperatures.

XRD patterns of $LiMnPO_4$/C materials synthesized at 550, 600, 650, and 700℃ (marked as LMP/C-550, LMP/C-600, LMP/C-650 and LMP/C-700, respectively.) are shown in Fig. 2b. It can be seen clearly that all the diffraction peaks of the samples match well with standard $LiMnPO_4$ (JCPDS: 33-0804) and show no evidence of the impurity phase, also confirming the formation of pure $LiMnPO_4$. Moreover, the diffraction peaks intensity of the samples increase significantly when the sintering temperatures is raised, indicating that the crystallinity of the synthesized material is improved. In addition, no carbon peaks is observed due to its amorphous form in the samples [30].

Fig. 3a-d show the SEM images of $LiMnPO_4$/C materials synthesized at different temperatures. In contrast to the $Mn_3(PO_4)_2 \cdot 3H_2O$ precursor with the morphology of nano-plate, the $LiMnPO_4$/C samples show an extremely high structural diversity comprising plate-like, spherical, rod-like and irregularly shaped forms. Moreover, It is also found that the content of plate-like particles decrease while the irregularly shaped particles increase with the rise of sintering temperature, indicating that the nanoplates of the $Mn_3(PO_4)_2 \cdot 3H_2O$ precursor were partly broken down to irregularly shaped smaller particles with main particle size in the range of 50~300 nm for $LiMnPO_4$/C during the sintering process. To further understand the microstructure of the composites, the sample synthesized at 650℃ is selected to be characterized by TEM (Fig. 3f). As shown in Fig. 3f, the LMP/C particles present an irregular shape with a size ranging from 50 to 150 nm, which is well consistent with the result of the SEM (Fig. 3c). And the BET specific surface area of LMP/C-550, LMP/C-600, LMP/C-650 and LMP/C-700 are measured to be 25.3, 36.4, 47.2 and 28.6 $m^2\ g^{-1}$, respectively. In comparison with these other three samples, sample LMP/C-650 shows the lowest agglomeration degree and the largest BET area. For LMP/C-700, the decrease in BET area when compared with LMP/C-650 indicates that it has a larger average particle size, which can be confirmed by the SEM image (Fig. 3d) and may result from the obvious growth of the particles synthesized at 700℃. Moreover, the larger specific surface area of LMP/C-650 is more advantageous in facilitating the penetration of the electrolyte to the surface of active particles that has a beneficial effect on electrochemical performance.

In order to further explore the morphology transformation of samples during the sintering process, bare $LiMnPO_4$ was synthesized following the same route with LMP/C-650 except that no glucose was added. As shown in Fig. 3e, we can see that the bare $LiMnPO_4$ particles are severely agglomerated and the average diameter of the particles is about 1um, which is almost seven times larger than that of LMP/C-650.

Hence, on the basis of the morphological study, it can be deduced that glucose has two effects on the sizes formation of the $LiMnPO_4$/C composite. One is that glucose adsorbed on the surface of the raw materials, namely, $Mn_3(PO_4)_2 \cdot 3H_2O$, $NH_4H_2PO_4$ and Li_2CO_3, and prevented the aggregation of the materials during the sintering process accompanied with the morphology transformation. The other is that the carbonization of glucose leads to the carbon coating on the surface of $LiMnPO_4$. As shown in Fig. 3g-h, the carbon coating layers with about 2nm thickness exist uniformly across the surface of the well-crystallized particles and connect the $LiMnPO_4$ particles (Fig. 3g-h), resulting in the inhibition of particles growth and formation of bridges among the $LiMnPO_4$ particles as well as providing a functional pathway for electron transportation. Moreover, it can be clearly seen from the HRTEM images (Fig. 3g-h) that the interplanar distances of 0.28, 0.23 and 0.37 nm correspond to the (301), (002) and (011) planes of the $LiMnPO_4$, respectively.

To evaluate the effect of sintering temperature on the electrochemical performance of $LiMnPO_4$/C, the 0.05C charge-discharge capacities of samples synthesized at various sintering temperatures are compared in Fig. 4a. All of the discharge curves show an obvious voltage plateau around 4.0 V corresponding to the

$MnPO_4/LiMnPO_4$ phase transformation. However, the plateau for LMP/C-650 occurs at the highest potential (~4.1 V) while that of LMP/C-550 occurs at the lowest potential (~3.9 V), which relates to the different electrochemical polarization degrees of these electrodes. The initial discharge capacity of the LMP/C-650 is 141.7 mAh g^{-1} at rate of 0.05 C, whereas that of the samples sintered at 550, 600 and 700℃ are 113.36, 129.6 and 120.5 mAh g^{-1}, respectively. In addition, the rate capacities of all samples at various rates from 0.05 C to 10 C are plotted in Fig. 4b. The $LiMnPO_4$/C prepared at 650℃ exhibits the highest discharge capacity accompanied with the longest discharge voltage plateau and the best rate capability. In order to further understand the excellent rate performance of LMP/C-650, Raman measurements were carried out. Shown in Fig. 4c is the Raman spectrum of LMP/C samples synthesized at various temperatures. It can be clearly seen that four samples exhibit two main peaks at 1340 and 1585 cm^{-1}, which correspond to the disordered (D) and graphite (G) bands of carbon, respectively [32]. The observed peaks at 946 cm^{-1} can be attributed to the PO_4^{3-} for $LiMnPO_4$ [33], and theirs intensity increase obviously when the sintering temperature is raised, which support a very good agreement with the XRD results. The full widths at half maximum (FWHM) of both the D and G band is often used to evaluate the graphitization degree of carbon and a smaller FWHM generally indicates higher graphitization degree [34]. Notably, the FWHM for four samples reduces successively from LMP/C-550, LMP/C-600, LMP/C-650 to LMP/C-700. This suggests that the graphitization degree of carbon in LMP/C samples increased with the increasing of the sintering temperature. Commonly, it is widely accepted that

the higher the graphitization degree of carbon, the higher of its electronic conductivity [34]. Compared with LMP/C-550 and LMP/C-600, carbon in LMP/C-650 samples with apparently higher degree of graphitization is more advantageous in increasing the electron conductivity of the LMP/C composites. Combined with the former structure discussion, morphological study and BET analysis, it is possible to come to a conclusion that the proper crystallinity, small particles with low agglomeration degree, large BET area, and well-distributed coating carbon with high graphitization degree, might account for the excellent electrochemical performance of LMP/C-650. In the case of LMP/C-700, it has the almost identical Raman spectra and even a higher degree of graphitization in comparison with LMP/C-650, however, the discharge capacity of LMP/C-700 is even worse than that of LMP/C-600, this is probably due to the serious agglomeration and apparent growth of particles at the higher sintering temperature, as shown in Fig. 3d.

Fig.4d shows the typical discharge curves of LMP/C-650 at various rates. The initial discharge capacities are 141.7 and 133.5 mAh g^{-1} at rates of 0.05 and 0.2C, respectively, which is superior to many other results [25, 28]. With the gradual increase of discharge current, the specific capacity decreased gradually and the discharge voltage plateau became short induced by the restricted Li-ion diffusion [35]. It exhibits discharge capacities of 126.6, 119.9 and 109 mAh g^{-1}, when the discharge rate increased to 0.5, 1 and 2 C, respectively. At the high current rates of 5 C and 10 C, specific capacities of 88.7 and 56.6 mAh g^{-1} are obtained, corresponding to 62.5% and 39.9% of its initial discharge capacity at 0.05C. Moreover, the distinct potential

plateaus can still retain even at the high rate of 5 C, indicating a small polarization loss. In comparison with the previously reported results [25, 28, 29], LMP/C-650 exhibits a superior rate performance, which indicates that the Li-ions diffusion is fast during charge-discharge process. Furthermore, the cycling performance of LMP/C-650 is shown in Fig.4e. The 100th discharge capacity of the LMP/C-650 at 0.5 C is 120.5 $mAh \cdot g^{-1}$, which is 95.2% of the initial capacity. The above results clearly suggest that the LMP/C-650 exhibits excellent rate capability and quite good cycle stability. These can be ascribed to the following two factors. Firstly, by comparison with the LMP/C-550 and LMP/C-600 samples, the better crystallinity and higher coating carbon graphitization degree of LMP/C-650 ensure both of Li-ion diffusion and electronic transmission at higher rate during the electrochemical reaction. Secondly, the LMP/C-650 possesses the largest specific surface area and the lowest particle agglomeration degree, which are beneficial to the wettability of the active materials with electrolyte, and facilitate the penetration of electrolyte inside secondary particles as well as accelerate the Li-ion transportation into/out of the electrode.

The cyclic voltammetry (CV) measurements were conducted to further evaluate the reversibility of the electrochemical reaction of the $LiMnPO_4$/C samples during charge-discharge process. Fig. 5a-d presents the typical CV curves of the LMP/C-650, LMP/C-600, LMP/C-700 and LMP/C-550 at different scan rates (0.1, 0.2 0.3 and 0.5 mV S^{-1}) between 2.5 and 4.5V. With increasing the scan rate, the anodic peaks shift to the high potential direction while cathodic peaks shift to the low potential,

accompanied by an increase in the intensity and area of redox peaks. However, it can be clearly seen that the anodic peaks are not detected at high scan rates (0.3 and 0.5 mV S^{-1}) for LMP/C-700 and even all the scan rates for LMP/C-550 due to the large electrochemical polarization. In comparison, for sample LMP/C-650, the area of cathodic peak is equal to that of the corresponding anodic peak for each plot, and the peak separation for each plot is apparently smaller than that of other three samples, which is indicative of the best reversibility and lowest electrochemical polarization. Moreover, the perfect linear relationship between the peak current (I_p) and the square root of the scan rate ($v^{1/2}$) suggests that the electrochemical process is purely limited by diffusion (Fig. 5e) [36]. Hence, the apparent lithiumion diffusion coefficient D (cm^2 s^{-1}) can be calculated according to the Randles-Sevcik equation [37]:

$$I_p = 0.4463 mAF^{3/2} R^{-1/2} T^{-1/2} C D^{1/2} n^{3/2} v^{1/2} \quad (3)$$

Where I_P is the peak current (A) at different scan rates, m is the mass of the electrode (g), A is the effective area of electrode (cm^2), F is the Faraday constant (96485 C mol^{-1}), R is the gas constant (8.314 J mol^{-1} K^{-1}), T is the absolute temperature (298 K), C is the concentration of Li ion in the cathode (mol ml^{-1}), n is the number of electrons transferred and v is the scanning rate (V S^{-1}). According to the slopes of the fitting lines in Fig. 5e, chemical diffusion coefficients of the Li-ion of LMP/C-550, LMP/C-600, LMP/C-650 and LMP/C-700 are calculated to be 5.47×10^{-15}, 1.46×10^{-14}, 2.25×10^{-14} and 8.36×10^{-15} cm^2 s^{-1}, respectively. Notably, the LMP/C-650 exhibited the largest Li-ion diffusion rate, endowing it with the best intrinsic kinetic properties and electrochemical performance. The reported diffusion

coefficients of the Li-ion vary from 10^{-12} to 10^{-16} cm^2 s^{-1}, based on the different calculation methods, test modes, etc. [38-39]. However, it is wildly accepted that better crystallinity, less defects and small size are very beneficial for increasing the diffusion values and improving the electrochemical properties [40]. LMP/C-650 shows the better crystallinity than LMP/C-550 and LMP/C-600 samples, and the smaller particle size than LMP/C-700, which might account for the largest Li-ion diffusion rate, best intrinsic kinetic properties and electrochemical performance.

4. Conclusions

Plate-like $Mn_3(PO_4)_2 \cdot 3H_2O$ precursor was synthesized by a novel precipitation process using ethanol as initiator and was lithiated to $LiMnPO_4$/C composite by a combination of wet ball-milling and heat treatment with glucose as the carbon source. The morphology of $Mn_3(PO_4)_2 \cdot 3H_2O$ precursor changed from plate-like into irregular structure and the size became smaller for the $LiMnPO_4$/C composite during the heat treatment process. The $LiMnPO_4$/C composite synthesized at 650℃ shows excellent electrochemical performance, and its discharge capacity is about 141.7, 133.5, 126.6, 119.9, 109, 88.7 and 56.6 mAh g^{-1} at rates of 0.05, 0.2, 0.5, 1, 2, 5 and 10 C, respectively. The cell retains 95.2% of its initial discharge capacity after 100 cycles at 0.5 C.

Acknowledgements

This work was supported by the Nature Science Foundation of Hunan province (Grant No.2015JJ3152), Fundamental Research Funds for the Central Universities (2012QNZT018), and China Postdoctoral Science Foundation (2012M521546).

References

[1] A.K. Padhi, K.S. Nanjundaswamy, J.B. Goodenough, J. Electrochem. Soc. 144 (1997) 1188-1194.

[2] T.H. Kim, H.S. Park, M.H. Lee, S.Y. Lee, H.K. Song, J. Power Sources 210 (2012) 1-6.

[3] S.M. Oh, S.T. Myung, Y.K. Sun, J. Mater. Chem. 22 (2012) 14932-14937.

[4] M. Minakshi, P. Singh, D. Appadoo, D.E. Martin, Electrochim. Acta 56 (2011) 4356-4360.

[5] Y.T. Cui, N. Xu, L.Q. Kou, M.T. Wu, L. Chen, J. Power Sources 249 (2014) 42-47.

[6] L. Chen, Y.Q. Yuan, X. Feng, M.W. Li, J. Power Sources 214 (2012) 344-350.

[7] Z.H. Chen, J.R. Dahn, J. Electrochem. Soc. 149 (2002) A1184-A1189.

[8] X.L. Pan, C.Y. Xu, D. Hong, H.T. Fang, L. Zhen, Electrochim. Acta 87 (2013) 303-308.

[9] S.M. Oh, S.W. Oh, S.T. Myung, S.M. Lee, Y.K. Sun, J. Alloys Compd. 506 (2010) 372-376.

[10] C. Delacourt, L. Laffont, R. Bouchet, C. Wurm, J.B. Leriche, M. Morcrette, J.M.Tarascon, C. Masquelier, J. Electrochem. Soc. 152 (2005) A913-A921.

[11] K.P. Wu, G.R. Hu, K Du, Z.D. Peng, Y.B. Cao, Mater Lett 152 (2015) 217-219.

[12] T. Shiratsuchi, S. Okada, T. Doi, J.I. Yamaki, Electrochim. Acta 54 (2009) 3145-3151.

[13] D. Wang, H. Buqa, M. Crouzet, G. Deghenghi, T. Drezen, I. Exnar, N.-H. Kwon, J.H. Miners, L. Poletto, M. Grätzel, J. Power Sources 189 (2009) 624-628.

[14] J.W. Lee, M.S. Park, B. Anass, J.H. Park, M.S. Paik, S.G. Doo, Electrochim. Acta 55 (2010) 4162-4169.

[15] J.K. Kim, C.R. Shin, J.H. Ahn, A. Matic, P. Jacobsson, Electrochem. Commun. 13 (2011) 1105-1108.

[16] M. Piana, B.L. Cushing, J.B. Goodenough, N. Penazzi, Solid State Ionics 175 (2004) 233-237.

[17] H. Fang, L. Li, Y. Yang, G. Yan, G. Li, Chem. Commun. (2008) 1118-1120.

[18] M. Zhao, Y. Fu, N. Xu, G. Li, M. Wu, X. Gao, J. Mater. Chem. A 2 (2014) 15070-15077.

[19] Y.T. Cui, N. Xu, L.Q. Kou, M.T. Wu, L. Chen, J. Power Sources 249 (2014) 42-47.

[20] F. Wang, J. Yang, P.F. Gao, Y.N. NuLi, J.L. Wang, J. Power Sources 196 (2011) 10258-10262.

[21] Y. Wang, Y. Yang, Y. Yang, H. Shao, Solid State Commun. 150 (2010) 81-85.

[22] B.J. Boonchom, S. Youngme, S.T. Maensiri, C.P. Danvirutai, J. Alloys Compd. 454 (2008) 78-82.

[23] B. Boonchom, R. Baitahe, Z.P. Joungmunkong, N. Vittayakorn, Powder Technol. 203 (2010) 310-314.

[24] J. Zong, Q.W. Peng, J.P. Yu, X.J. Liu, J. Power Sources 228 (2013) 214-219.

[25] N.N. Bramnik, H. Ehrenberg, J. Alloys Compd. 464 (2008) 259-264.

[26] L. Wang, W.T. Sun, X.M. He, J.J. Li, C.Y. Jiang, J. Electrochem. Soc. 6 (2011) 2022.

[27] J. Xiao, N.A. Chernova, S. Upreti, X. Chen, Z. Li, Phys. Chem. Chem. Phys. 13 (2011) 18099.

[28] J.L. Liu, D.G. Hu, T. Huang, A.S. Yu, J. Alloys Compd. 518 (2012) 58-62.

[29] H.J. Zhu, W. Zhai, M. Yang, X.M. Liu, Y.C. Chen, H. Yang, X.D. Shen, RSC Adv. 4 (2014) 25625-25632.

[30] Y.B. Cao, J.G. Duan, G.R. Hu, F. Jiang, Z.D. Peng, K. Du, H.W. Guo, Electrochim. Acta 98 (2013) 183-189.

[31] A.A. Thorat, S.V. Dalvi, Chem. Eng. J. 181-182 (2012) 1-34.

[32] A.C. Ferrari, J. Robertson, Phys. Rev. B 61 (2000) 14095-14107.

[33] Y. Zhang, W.C. Wang, P.H. Li, Y.B. Fu, X.H. Ma, J. Power Sources 210 (2012) 47-53.

[34] X. Zhou, F.Wang, Y.Zhu, Z.Liu, J. Mater. Chem. 21 (2011) 3353-3358.

[35] W.X. Zhang, Z.Q. Shan, K.L. Zhu, S.Z. Liu, X.Y. Liu, J.H. Tian, Electrochim. Acta 153 (2015) 385-392.

[36] L. Li, X. Tang, H. Liu, Y. Qu, Z. Lu, Electrochim. Acta 56 (2010) 995-999.

[37] S. Yang, X. Zhou, J. Zhang, Z. Liu, J. Mater. Chem. 20 (2010) 8086-8091.

[38] Y.R. Wang, Y.F. Yang, X. Hu, Y.B. Yang, H.X. Shao, Solid State Commun. 150 (2010) 81-85.

[39] V. Ramar, K. Saravanan, S.R. Gajjela, S. Hariharan, P. Balaya, Electrochim. Acta 105 (2013) 496-505.

[40] H. Guo, C.Y. Wu, J. Xie, S.C. Zhang, G.S. Cao, X.B. Zhao, J. Mater. Chem. A 2 (2014) 10581.

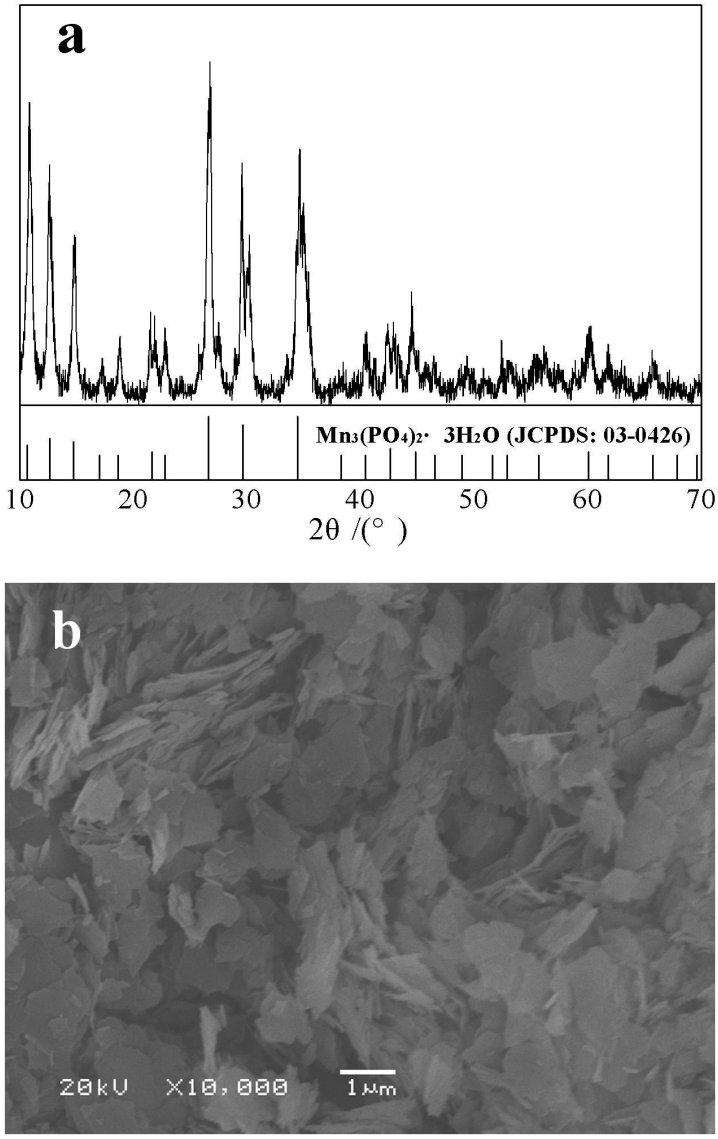

Fig. 1 XRD pattern (a) and SEM image (b) of as-prepared $Mn_3(PO_4)_2 \cdot 3H_2O$.

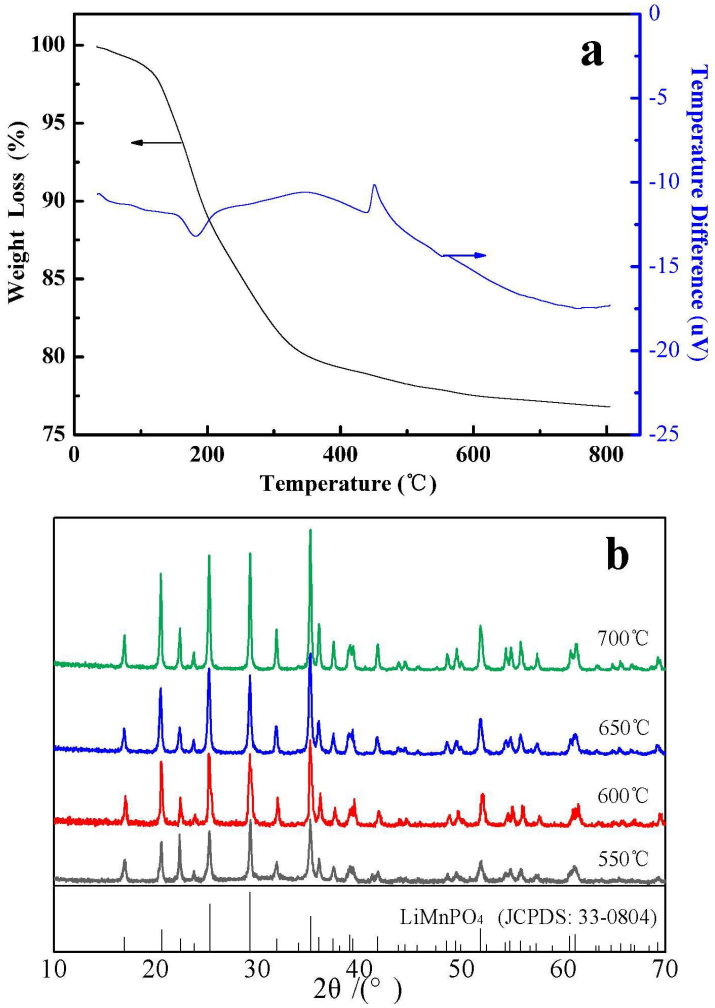

Fig. 2 (a) TGA-DSC curves of the ball-milled mixture of $Mn_3(PO_4)_2 \cdot 3H_2O$, $NH_4H_2PO_4$, Li_2CO_3 and glucose; (b) XRD patterns of $LiMnPO_4$/C synthesized at different temperatures.

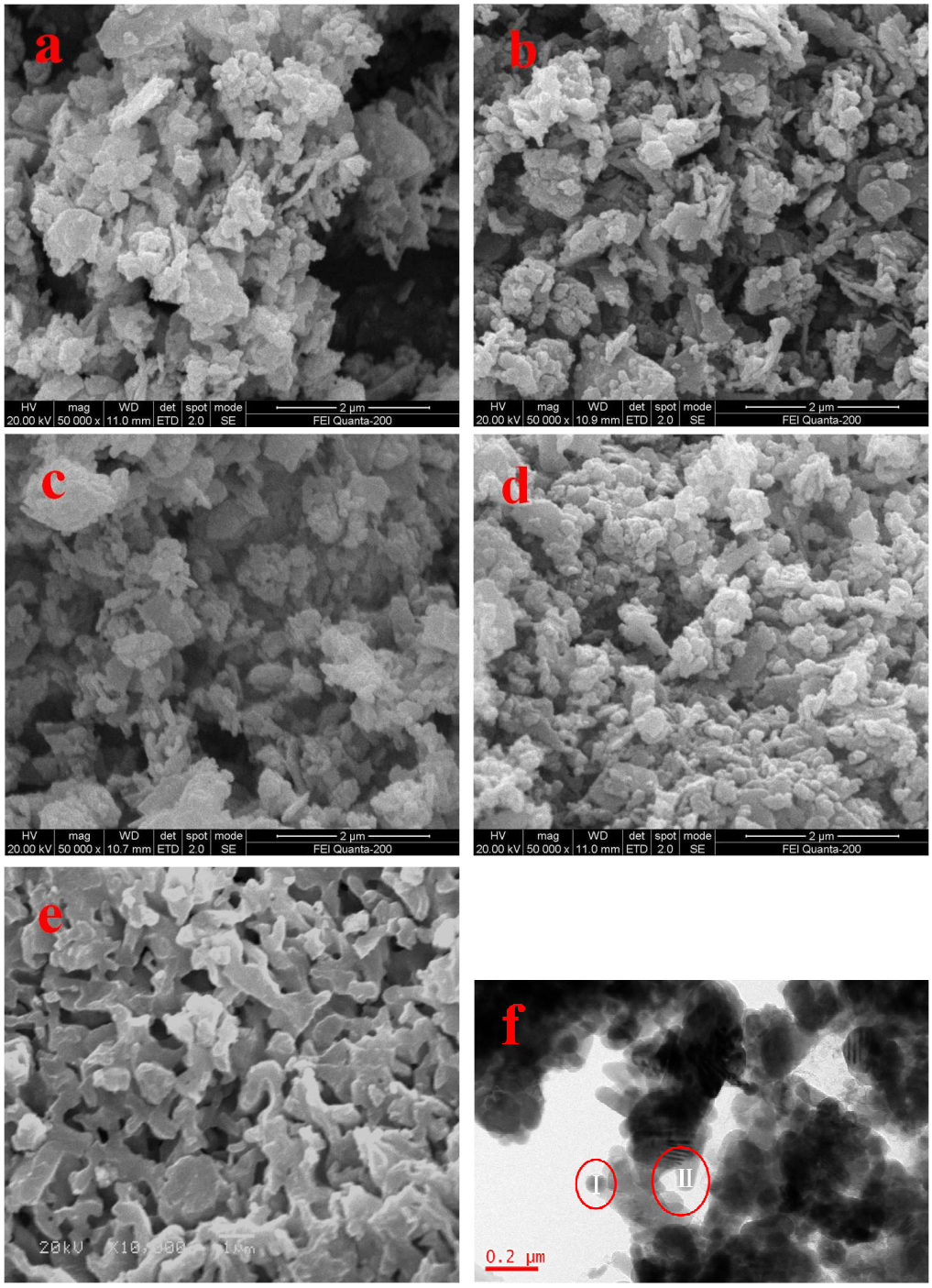

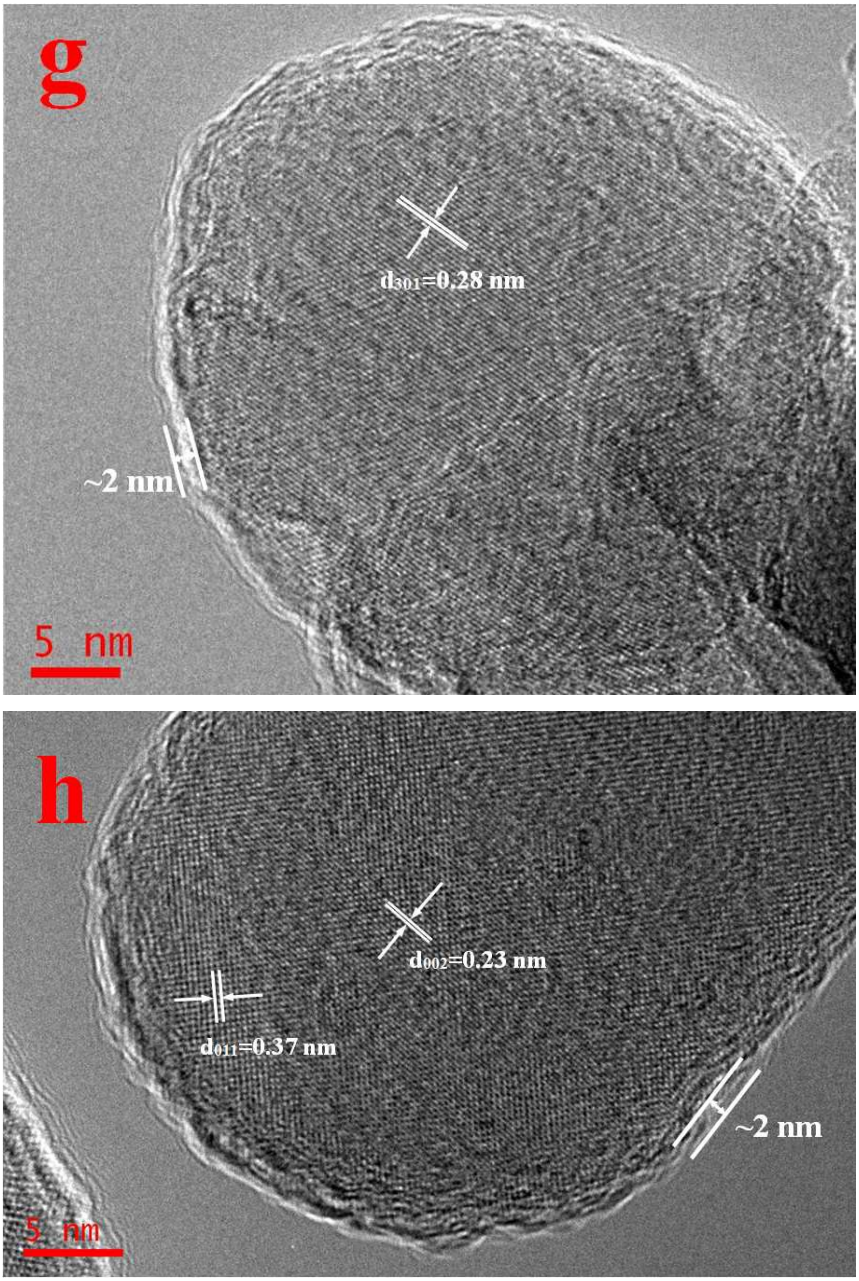

Fig. 3 SEM images of $LiMnPO_4$/C synthesized at different temperatures (a) 550℃, (b) 600℃, (c) 650℃ and (d) 700℃; SEM image of bare $LiMnPO_4$ (e); TEM (f) and HRTEM (g and h) images of LMP/C-650.

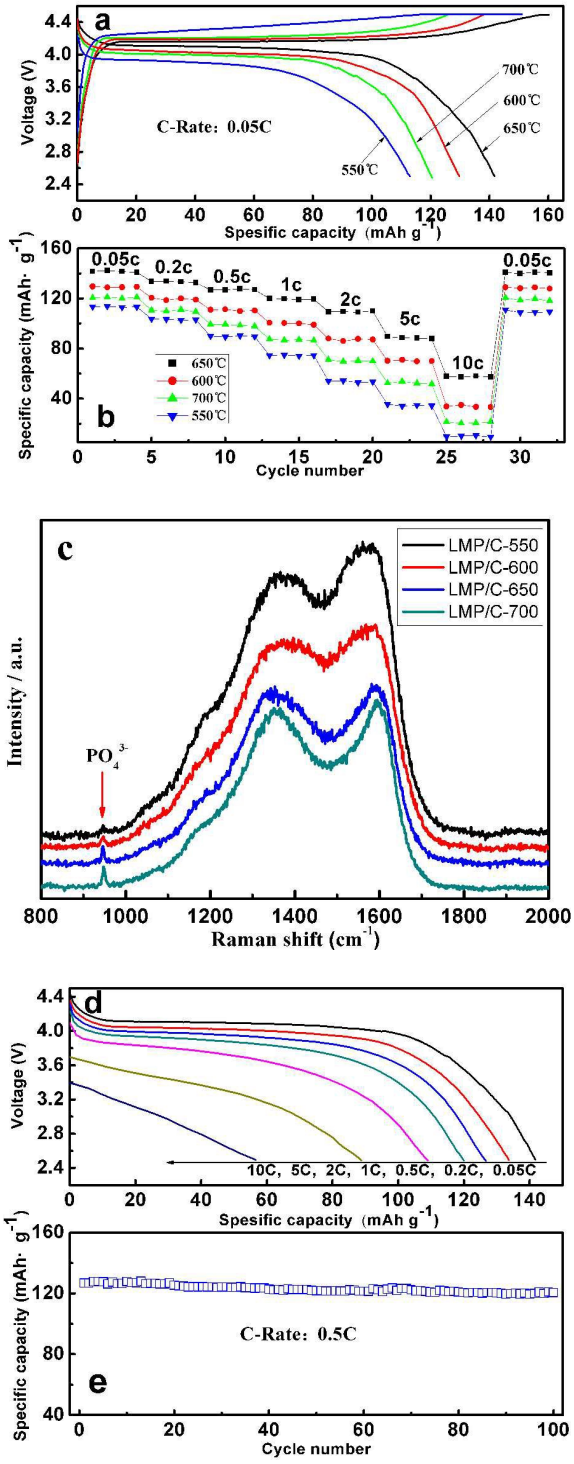

Fig. 4 (a) The 0.05C charge-discharge capacities of samples synthesized at various heating temperatures; (b) Rate performance and (c) Raman spectra of $LiMnPO_4$/C samples; (d) Discharge curves and (e) Cycling performance of LMP/C-650;

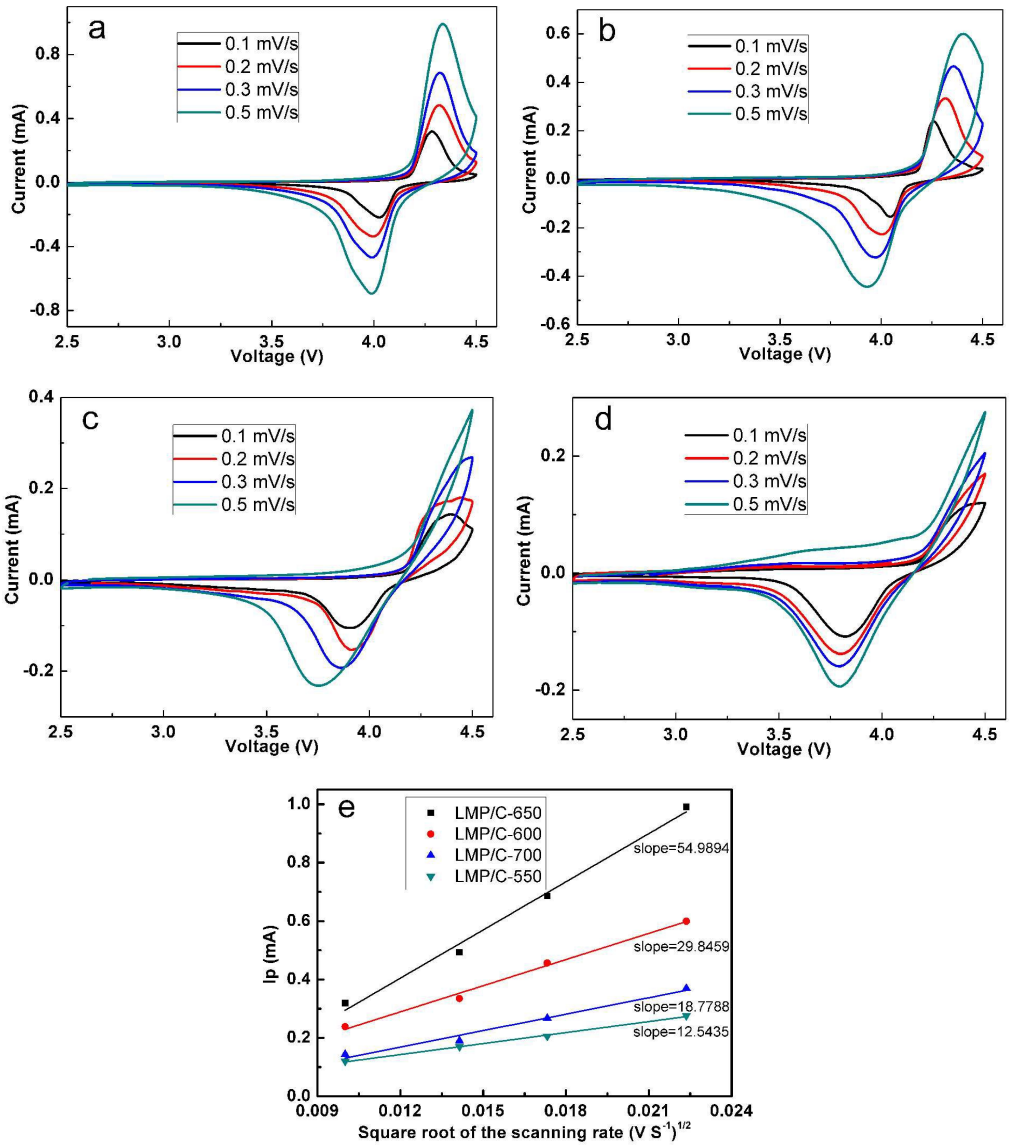

Fig. 5 CV curves of LMP/C-650 (a), LMP/C-600 (b), LMP/C-700 (c) and LMP/C-550 (d) at different scanning rates; (e) Relationship between the peak current and the square root of the scanning rate.

Graphical Abstract